Bubble characteristics and trajectories in a microbubble boundary layer

S. Pal, C. L. Merkle, and S. Deutsch
Department of Mechanical Engineering and The Applied Research Laboratory, Pennsylvania State University, University Park, Pennsylvania 16802

(Received 15 August 1987; accepted 21 December 1987)

Optical and photographic surveys of microbubble boundary layers are presented. The results show that the outer edge of the bubble cloud diffuses away from the wall as the bubbles are swept downstream. The plate-on-bottom orientation contains a bubble-free region near the wall that cannot be discerned for the plate-on-top configuration. Skin friction measurements made when the bubble-free region extends to $y^+ = 200$ show there is no longer any C_f reduction present suggesting bubbles are not effective when they are outside the near-wall region of the boundary layer. Bubble sizes, which increase with airflow and distance from the injection section and decrease with free-stream velocity, were measured to be between 150 and 1100 μm.

I. INTRODUCTION

The control of skin friction drag has been the subject of numerous investigations in both laminar and turbulent flows. The present paper deals with a concept for controlling turbulent shear stress in liquid boundary layers through the introduction of a large concentration of small bubbles ("microbubbles"). Investigations into microbubble drag reduction started with McCormick and Bhattacharyya's total drag measurements on a towed body of revolution.[1] These experiments were followed by a series of skin friction measurements on flat plates by Soviet researchers[2–5] and more recently by similar experiments in our laboratory.[6–9] A summary of much of this work is given in Ref. 10. Preliminary attempts at modeling the phenomenon are given in Refs. 11 and 12.

The flat plate experiments conducted by the Soviets[2–5] showed that local C_f reductions of as much as 90% could be obtained over a range of flow conditions. In general, the C_f reduction increased with airflow rate until some maximum "saturation" level was reached. These results were extended in numerous ways including wider velocity ranges, different gravitational orientations, additional types and sizes of porous surfaces, and both flat plate and axisymmetric geometries by the measurements in our laboratory.[6–9] Taken together, these two sets of measurements demonstrate reasonably well the range of parameters over which reduced skin friction can be attained by introduction of microbubbles to a laboratory boundary layer.

Although the effectiveness of microbubble injection has been demonstrated, the mechanisms that lead to this reduction are not completely understood and, consequently, practical problems such as air optimization and scale-up cannot be sensibly addressed. What is particularly lacking is an understanding of the interaction between the bubbles and the boundary layer. The measurements described in this paper represent new information on bubble/boundary-layer interaction that should be an important guide to future modeling studies.

II. EXPERIMENTAL FACILITY

The results given in the present paper were taken on a flat plate mounted in the round test section of the 12 in. water tunnel at the Pennsylvania State University. The previously reported flat plate measurements[6–8] were made on one wall of the rectangular test section of the same tunnel. The new experimental arrangement was chosen because it allows much improved optical access.

The flat plate is 1100 mm in length, is centered in the test section, and spans the width of the tunnel. Air is injected through a 76×51 mm porous section flush mounted on the surface of the plate. The leading edge of the porous section is 254 mm downstream of the leading edge of the plate as indicated in Fig. 1. The porous filter material used for these experiments was a 3 mm thick piece of sintered stainless steel with a nominal filter size of 40 μm. It has been shown previously that pore size has only a weak effect on the skin friction reduction.[7]

The entire test section can be rotated enabling the study of gravitational effect. We refer to the orientation in which buoyancy causes the bubbles to rise out of the boundary layer as the "plate-on-bottom" case, while for the "plate-on-top" case, the tunnel has been rotated 180°. The tunnel has a 0.2 m^3/sec bypass system that removes a substantial fraction of the recirculating water from the closed circuit tunnel and replaces it with fresh water, a process necessary for keeping the free stream relatively bubble-free.

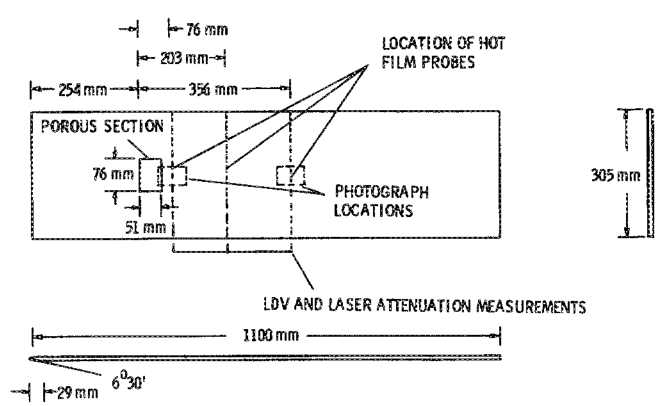

FIG. 1. Schematic of the flat plate showing location and size of porous section and instrumentation locations for LDV measurements, flush-mounted hot-film probes, and top and side view photographs.

 0031-9171/88/040744-08$01.90

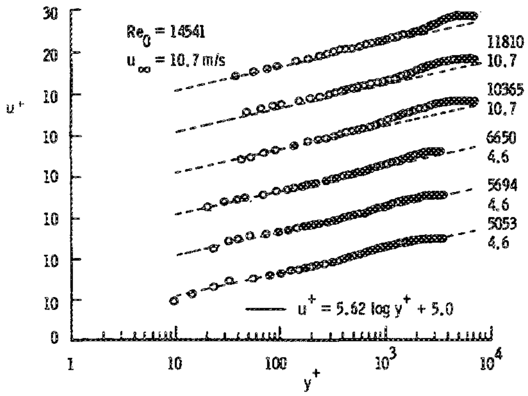

FIG. 2. LDA velocity profile measurements in the undisturbed boundary layer presented in inner variables. Note shifted origins.

The undisturbed boundary layer was characterized by pressure distribution and velocity profile measurements. Surface pressure taps at 40 locations on the plate were used to demonstrate that the flow field was at nominally zero pressure gradient except within the first 25 mm of the leading edge. Laser Doppler velocimetry measurements at two velocities (4.6 and 10.7 m/sec) were made at the three locations shown in Fig. 1. Velocity profiles for these two speeds are shown in inner variables in Fig. 2. These results show that the boundary layer is reasonably close to a classical, equilibrium turbulent boundary layer.

Measurements of the bubble characteristics were made at the same three locations and the same two tunnel velocities as the LDV studies. To quantify the C_f reductions corresponding to these bubble observations, hot-film gauges were flush-mounted on the surface of the plate at these same three locations. The probes were calibrated using the technique described in Ref. 8. The general trends of these skin friction measurements as a function of airflow rate for the two test velocities are quite similar to those presented in Ref. 8. The magnitude of the C_f reduction at six specific airflow rates is given in Table I. These six rates are the ones at which the photographs and bubble cloud location measurements were made, and are referred to throughout as rates I–VI. Both dimensional airflows and approximate volumetric airflow rates (Ref. 10) are given. Airflow rates I and II correspond to negligible C_f reductions, while rates III–VI correspond to moderate to large reductions. The extremely low values ($<10\%$) of C_f/C_{f0} for rate IV should be looked at as being only indicative of large C_f reductions as the calibration is uncertain at these low levels.

III. GENERAL CHARACTERISTICS OF THE BUBBLE FLOW FIELD

Air injected into the boundary layer through the injection section is rapidly broken into small bubbles that are then swept downstream. A series of photographs were taken for the various airflow rates, locations, and plate orientations in an attempt to provide a general qualitative picture of the bubble flow field. The photographs were taken with a 35 mm camera using a 55 mm Nikon lens and Kodak Tri-X, 20 exposure film. Top lighting was used for both side and top views. Lighting was obtained from a stroboscope with a flash duration of 40 μsec.

The most striking aspect of the photographs is that even those airflow rates that provide only small reductions in C_f correspond to conditions in which the bubbles appear as a cloud rather than as isolated bubbles. This makes it difficult to obtain quantitative information on individual bubble characteristics. Some important qualitative characteristics can, however, be discerned. Analysis of the sequence of photographs shows that, as in the case of single pore injection,[13,14] bubble size increases with airflow rate and with speed reduction. Moreover, the photos show clear evidence of bubble coalescence with downstream distance.

Quantitative measurements of bubble sizes and comparisons with appropriate turbulence and boundary-layer

TABLE I. Airflow rate classifications and corresponding skin friction results.

Airflow rate	Dimensional airflow ($\times 10^{-3}$ m^3/sec)	Volumetric airflow ratio $Q_A/(Q_A+Q_W)$ Vel = 4.6 m/sec	Vel = 10.7 m/sec	C_f/C_{f0} Free-stream velocity = 4.6 m/sec Top[a]/Bottom[a] $x = 76$ mm	Top[a]/Bottom[a] $x = 203$ mm	Top[a]/Bottom[a] $x = 356$ mm	Free-stream velocity = 10.7 m/sec Top[a]/Bottom[a] $x = 76$ mm	Top[a]/Bottom[a] $x = 203$ mm	Top[a]/Bottom[a] $x = 356$ mm
I	0.05	0.03	0.01	0.98 / 0.99	0.98 / 0.98	0.99 / 1.0	0.98 / 0.98	0.98 / 0.99	0.99 / 1.0
II	0.14	0.07	0.04	0.95 / 0.98	0.95 / 0.92	0.98 / 1.0	0.92 / 0.92	0.95 / 0.98	0.98 / 0.99
III	0.28	0.13	0.07	0.42 / 0.93	0.40 / 0.82	0.75 / 0.96	0.85 / 0.90	0.92 / 0.93	0.97 / 0.98
IV	0.46	0.19	0.11	0.05 / 0.51	0.04 / 0.92	0.08 / 0.91	0.58 / 0.78	0.86 / 0.90	0.92 / 0.94
V	1.13	0.37	0.23	/ 0.26	/ 0.29	/ 0.98	/ 0.12	/ 0.56	/ 0.82
VI	1.96	0.51	0.35	/ 0.18	/ 0.22	/ 1.01	/ 0.22	/ 0.11	/ 0.60

[a] Top and bottom signify plate-on-top and plate-on-bottom.

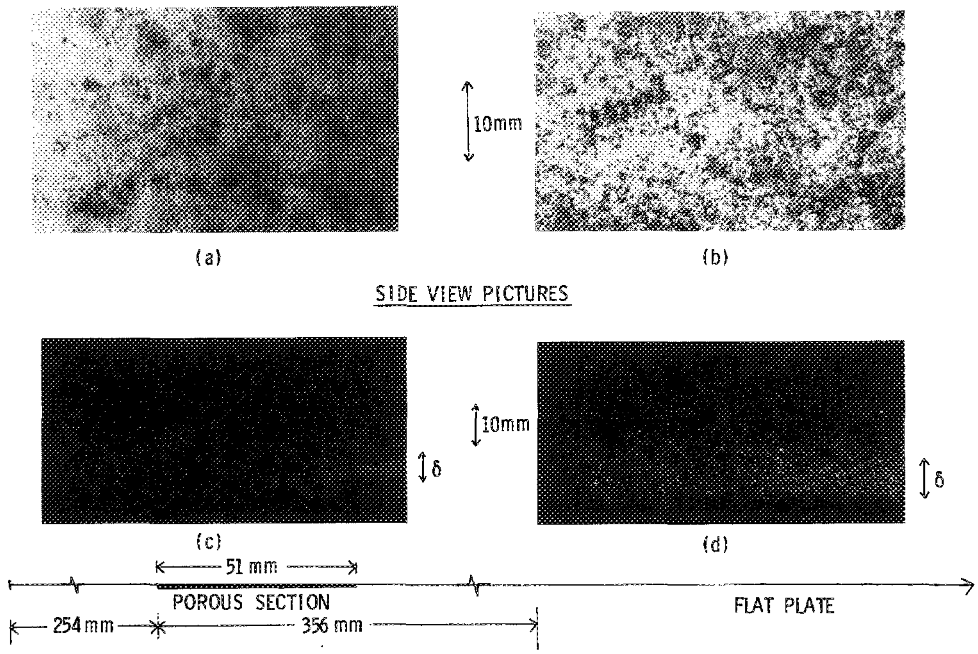

FIG. 3. Top [(a) and (b)] and side [(c) and (d)] view photographs depicting the evolution of the bubble cloud for airflow III at a velocity of 10.7 m/sec and for the plate-on-bottom orientation. Photographs (a) and (c) are at the injection location ($C_f/C_{f0} = 0.90$) and (b) and (d) are at a location 356 mm downstream from leading edge of porous section ($C_f/C_{f0} = 0.98$). A relative scale is marked for convenience.

scales, however, represent an essential ingredient for improving understanding of how bubbles affect the structure of a turbulent boundary layer. To date, no such measurements have been reported. To provide at least an order of magnitude estimate of bubble sizes, we have used photographs taken at the lower airflow rates (I, II) where the individual bubbles are distinguishable. Comparison of these photographs with those at higher airflow conditions (rates III–VI) clearly shows the bubble sizes are representative of those at conditions of interest (compare Figs. 3 and 4). Analytical bubble size estimates given later also justify this extrapolation in airflow rate.

IV. BUBBLE SIZE MEASUREMENTS

Bubble size measurements were made manually from top-view photographs like that shown in Fig. 4 by projecting the photos on the wall, marking the area, and counting and measuring the bubbles within that area. Typical sample sizes were from 50 to 100.

Bubble size measurements were made for both the 4.6 and 10.7 m/sec conditions and were obtained for both gravitational orientations. Both the near injector and the far downstream measurement location (see Fig. 1) were used. Synopses of the measurements are given in Fig. 5.

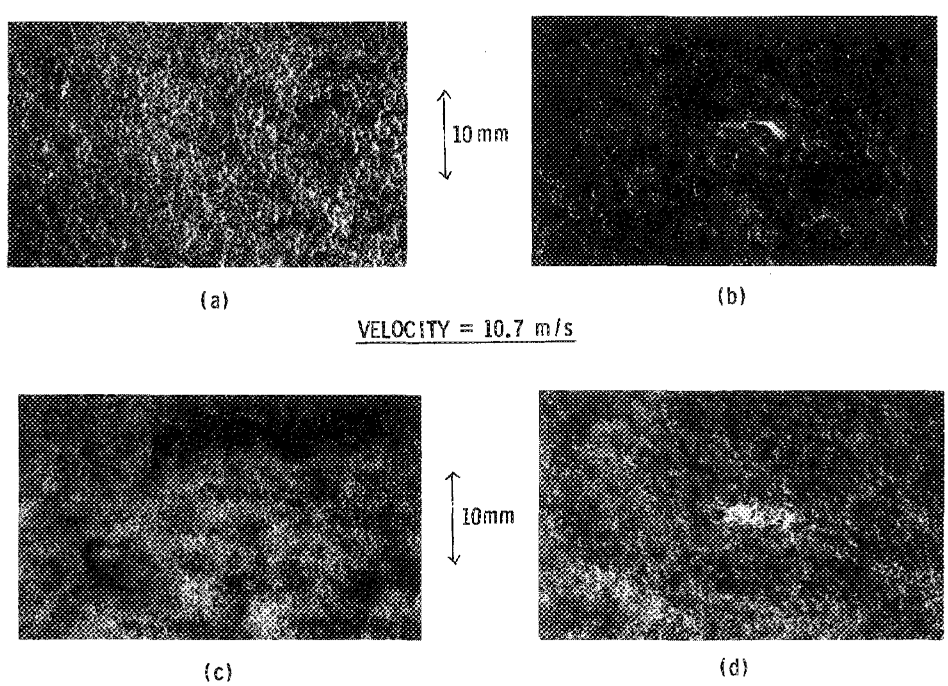

FIG. 4. Top view comparison of airflow II between a free-stream velocity of 4.6 m/sec (a) at injection location ($C_f/C_{f0} = 0.98$) and (b) 356 mm downstream from leading edge of porous section ($C_f/C_{f0} = 1.0$) and 10.7 m/sec (c) at injection location ($C_f/C_{f0} = 0.92$) and (d) 356 mm downstream from leading edge of porous section ($C_f/C_{f0} = 0.99$).

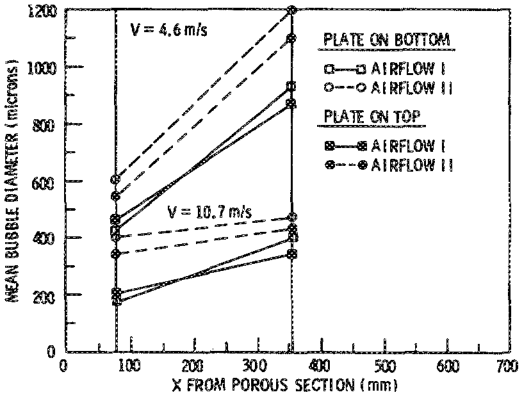

FIG. 5. Average bubble diameters as a function of airflow rate, velocity, plate orientation, and distance from injection section.

Several general conclusions can be drawn from the measurements. First, the average bubble size lies between 150 and 1200 μm, which is in reasonable agreement with the numbers calculated later. The smallest bubbles are still an order of magnitude larger than the sublayer thickness (about 10 μm here), while the largest are still an order of magnitude smaller than the boundary-layer thickness (about 10 mm here). This may help explain the relative insensitivity of the drag reduction phenomena that we have observed to changes in injection technique or surface tension (through the introduction of surfactant). Second, the qualitative increase in bubble size with distance from the injection section noted earlier is seen to approximately double the bubble size for these conditions. This relatively rapid growth in bubble size at low bubble densities would suggest inter-bubble interactions are quite significant in the bubble cloud regime. Third, differences between bubble sizes for the plate-on-top and plate-on-bottom configurations appear to be within the scatter of the data.

The bubble size measurements reported above make it interesting to speculate on the physics that controls the bubble sizes. Bubble sizes may be presumed to be determined by a competition among three events: bubble formation processes at injection, bubble splitting because of bubble turbulence interactions, and bubble coalescence arising from bubble collisions.

Initial estimates of bubble size based on Taylor instability of the individual bubbles[3] placed the bubble sizes at a few (two or three) microns and parallel reasoning suggested that diameters above 50 μm would lead to drag increases. The present measurements refute these arguments. Later estimates based on isolated pore injection[10] placed bubble sizes in the range of a few hundred microns (100–500 μm). These magnitudes are close enough to suggest that the formation process may have an impact on the observed bubble sizes, but the observed bubble growth with distance from the injection section indicates other processes must also be considered.

Hinze[15] was the first to consider the effect of turbulence on bubble size. By considering a balance between pressure and capillary forces for bubbles affected by turbulence on the scale of the inertial subrange, he determined that the maximum bubble size stable against breakup was

$$d_1 \sim (\sigma/\rho)^{3/5}\epsilon^{-2/5}, \tag{1}$$

where σ is the surface tension, ρ the liquid density, and ϵ the dissipation. In the boundary layer, we may write

$$\epsilon \sim u_*^3/\theta, \tag{2}$$

with u_* the shear velocity and θ the momentum thickness, a representative length scale. Using the definition of the friction velocity, this gives

$$d_1 \sim \tau_w^{-3/5}, \tag{3}$$

with τ_w the wall shear stress and the proportionality constant presumably of order 1.

Thomas[16] has extended this analysis to include bubble coalescence and finds that bubbles will coalesce for sizes smaller than

$$d_2 \sim (\sigma^2 h^2/\rho^2 \nu\epsilon)^{1/4}, \tag{4}$$

with ν the kinematic viscosity of the liquid and h the rupture thickness of the bubble. In the same way, then,

$$d_2 \sim \tau_w^{-3/8}. \tag{5}$$

We should note that time scales for both coalescence and breakup can also be estimated and show that for our flow conditions both occur within tenths of microseconds of injection.

Using Eqs. (3) and (5), we can estimate that for a factor of 2 decrease in the drag the breakup size d_1 would increase by about 50% while the coalescence size d_2 would increase by about 30%. This agrees with our earlier observations that bubble size increases with airflow rate, but also suggests that the use of bubble measurements at low values of C_f reduction should provide diameters that are within a factor of 2 of those at drag-reducing conditions. The bubble growth with distance from the injection location can also be explained on the basis of these analyses[15,16] if we recognize that bubble diffusion with distance moves the bubbles into the outer region of the boundary layer where ϵ is smaller.

Finally, if we take the proportionality constant in Eqs. (1) and (4) to be unity, we predict bubble sizes ranging from 500 to 1100 μm for the low speed case and from 50 to 500 microns for the high speed case. These estimates are close to our measurements. In summary, we find that both the bubble formation mechanisms and the bubble breakup estimates lead to size estimates that are near the measured values. The bubble growth coupled with the breakup/coalescence estimates suggests the bubble size may be the result of a dynamic process.

V. STREAMWISE TRAJECTORY OF THE BUBBLE CLOUD

To obtain information as to the bubble cloud location, the laser attenuation measurement shown schematically in Fig. 6 was devised. A 1 mm diameter beam from a low power He–Cd (325 nm) laser was passed through the bubble cloud perpendicular to the flow and was received by a photomultiplier on the opposite side of the tunnel. The combined laser–photomultiplier system was mounted on a precision jack

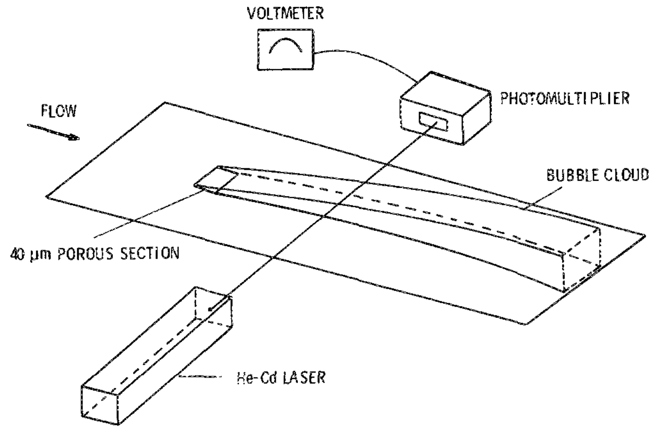

FIG. 6. Schematic of the laser attenuation procedure used to measure bubble cloud location and trajectory.

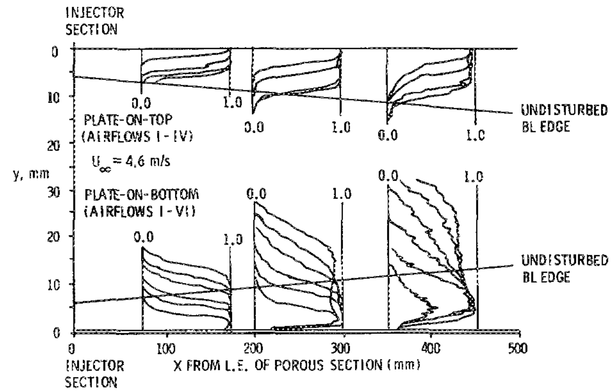

FIG. 7. Laser attenuation profiles for plate-on-bottom (lower half) and plate-on-top (upper half) at the three measuring stations (4.6 m/sec). Airflow rates I–VI are shown for the plate-on-bottom case and rates I–IV for plate-on-top. In all cases, the profile closest to the wall is profile I and succeeding profiles move monotonically away from the wall. The location of the injector section and the undisturbed boundary-layer edge are also shown.

that allowed traversing in the distance normal to the plate surface. The motion of the jack was monitored by a dial gauge with 0.0254 mm gradations.

To determine the location of the bubble cloud, the laser beam was typically traversed from the plate surface to the outer edge of the bubbles and back. In the center of a typical bubble cloud at concentration levels corresponding to significant C_f reduction, the laser beam was totally obscured. As the beam neared the outer edge of the cloud, beam transmission increased toward its level in clear water. In principle, the attenuation of the laser beam provides a measure of the integrated bubble characteristics along the line of sight of the beam. It is virtually impossible, however, to provide a calibration procedure to make such measurements quantitative even if the beam was not totally obscured much of the time. Such measurements can, however, still provide useful information about bubble dynamics.

Laser attenuation measurements were made at the three previously mentioned locations and the two tunnel velocities. For the plate-on-bottom orientation, measurements were made for airflow rates I–VI, while for the plate-on-top orientation, only airflows I–IV were measured. Percent laser attenuation traverses for both gravitational orientations are given in Fig. 7 for 4.6 m/sec. The figure has six embedded plots: the bottom three represent laser attenuation traverses at the three measuring stations for the plate-on-bottom configuration; the top three represent plate-on-top data at the same locations. The abscissas on these figures represent the distance along the flat plate measured from the leading edge of the injection section while the ordinates represent the distance normal to the plate surface (measured upward from the bottom and downward from the top). The location of the injection section and the undisturbed boundary-layer thickness along the plate are also included on the figure. The two vertical lines at each measurement station, marked 0.0 and 1.0, that enclose the attenuation profiles represent the photomultiplier output with the beam transmitting through clear water and its output with the beam turned off. Although the attenuation profiles cannot be directly converted to concentration profiles, the traverses at various airflow rates give a representative idea of the characteristics and location of the bubble cloud as it progresses downstream.

From the plate-on-bottom measurements on the bottom half of Fig. 7, we see that at the measuring station next to the injection section, the laser beam is completely attenuated near the wall for airflows II–VI. Only at the lowest airflow rate is the cloud marginally translucent at this location. Comparison of these six airflow rates shows that the transition from totally obscured to fully transmitting occurs farther away from the wall as the airflow is increased. The increased volume of bubbles pushes the outer edge of the bubbles farther from the wall encompassing a larger fraction of the boundary layer. (It is also likely that the local bubble concentration near the wall increases as the airflow rate is increased.) The amount of C_f reduction at this location ranges from 2%–80% depending on airflow as indicated in Table I.

As the bubbles move downstream from the injection section, significant changes in the attenuation profiles occur. At the middle measuring station ($x = 203$ mm) the profiles for the three lowest airflow rates show a zone of reduced attenuation next to the wall indicating that the bubble cloud is moving away from the wall at these flow rates. The outer edge of the profile is displaced considerably farther from the wall than it was at the upstream station. The plate-on-bottom attenuation profiles at the farthest location from the injection section ($x = 356$ mm) show even stronger evidence of reduced attenuation near the wall. Here, all six airflow rates show nearly zero attenuation next to the wall. Visual inspection at this plate-on-bottom location revealed a distinct clear water region between the bubble cloud and the wall, verifying that the entire bubble cloud was migrating away from the wall. Note that the bubble cloud is now translucent throughout its entire thickness at even the highest airflow rate.

The comparison of the corresponding plate-on-top laser attenuation profiles on the top half of Fig. 7 with these plate-on-bottom results allows us to make some additional observations. The plate-on-top data show no evidence of reduced transmission near the wall for any of the three measurement locations. (Recall, however, that the probe cannot resolve details at a sublayer scale.) Visual observations also failed to discern a clear water region next to the wall. The contrast in the plate-on-top and plate-on-bottom data clearly shows that buoyancy is the mechanism that causes the bubbles to move away from the wall.

The other major difference between the plate-on-top and plate-on-bottom data at 4.6 m/sec occurs in the outer edge of the bubble cloud. Comparing the profiles at the top of Fig. 7 shows that even when buoyancy inhibits movement away from the wall, the outer edge of the bubbles still diffuses away from the wall causing the cloud to become thicker as it moves downstream. The bubble diffusion rate is thus affected by turbulence as well as by buoyancy. Visual observations of single bubble injection into this same boundary layer have demonstrated that the trajectories of individual bubbles are strongly controlled by turbulence.

As an estimate of the effect of buoyancy, an isolated bubble rising at terminal velocity would rise a distance

$$\Delta y = (gd^2/36\nu)L/u_\infty \qquad (6)$$

as it was swept downstream through a distance L. Other parameters in Eq. (6) include the gravitational acceleration g and the free-stream velocity u_∞. We have assumed low Reynolds number flow and a bubble velocity of one-half u_∞. For the 4.6 m/sec condition in the present experiment, this means a 100 μm bubble would move 0.2 mm from the wall by the time it reaches the downstream station, while a 1000 μm bubble would rise 20 mm. These estimated rise distances are not unlike the diffusion rates noted in Fig. 7 and for bubble sizes of 200 or 300 μm would reasonably well justify that the diffusion were about equally split between gravity and turbulence as the figure suggests.

The corresponding laser attenuation profiles for the higher velocity (10.7 m/sec) case are shown in Fig. 8. The major difference between these traverses and those at the lower velocity is that the bubble cloud is thinner for this higher velocity. There are two reasons for this. The first is because the convection time is shorter so that bubble motion by buoyancy and turbulent diffusion is decreased. The second is that although the volumetric flow rate of air is the same for the two cases, the volumetric flow ratio of air to water is smaller at the higher speeds. Thus, for a given airflow rate, the relative concentration of bubbles is smaller at the higher speed. Referring to Table I, we see that approximately equal volume flow rates are obtained if we compare airflow II in Fig. 8 with airflow I in Fig. 7; airflow III with airflow II; airflow V with airflow IV; and airflow VI with airflow V. Comparisons at constant volumetric flow ratio makes the bubble profiles more nearly similar at the two speeds, particularly for the plate-on-top data. This also helps to explain why the volumetric flow ratio was found best in Ref. 10 at collapsing the drag reduction data.

VI. LASER ATTENUATION PLOTS IN INNER VARIABLES

To test the manner in which these laser "concentration" profiles scale, and to place them in more conventional turbulent boundary-layer notation, some of the results in Figs. 7 and 8 have been replotted in inner variables and are shown on Figs. 9–12. For brevity, only the plate-on-bottom results for the near injector location and the far downstream location are included. Results are shown for both the 4.6 and the 10.7 m/sec velocities. In determining y^+, the measured values of C_f in the presence of bubbles have been used.

At the near injector location and the lower speed, the outer edge of the bubbles extends to about $y^+ = 1000$ (see Fig. 9). Even in inner variables (note the effect of the bubbles on the shear stress causes the inner scale to increase as air is added), the outer edge of the bubbles generally moves farther from the plate as more air is added. Similar observations are true for the 10.7 m/sec case shown on Fig. 10 except that the outer edge grows to several thousand at the higher airflow rates. In both these cases, the resolution of the measurements is not sufficient to reveal the details of the bubble concentration profiles inside a y^+ value of about 100. All that can be concluded at both speeds is that bubbles are present at $y^+ = 100$ and extend outward beyond this location.

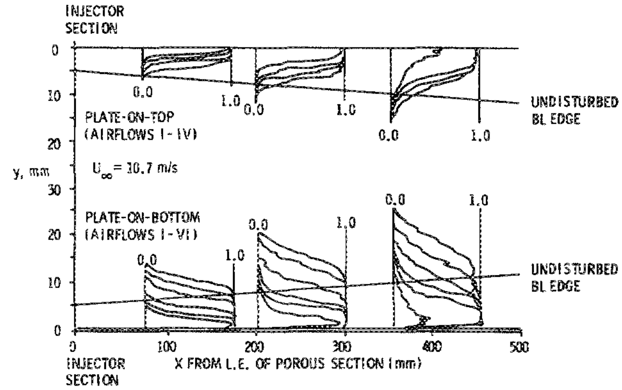

FIG. 8. Laser attenuation profiles for plate-on-bottom (lower half) and plate-on-top (upper half) at the three measuring stations (10.7 m/sec). Airflow rates I–VI are shown for the plate-on-bottom case and rates I–IV for plate-on-top. In all cases, the profile closest to the wall is profile I and succeeding profiles move monotonically away from the wall. The location of the injector section and the undisturbed boundary-layer edge are also shown.

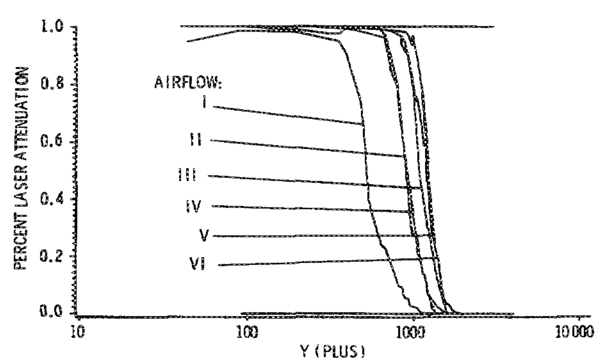

FIG. 9. Laser attenuation data as a function of y^+. Here, $u = 4.6$ m/sec; plate-on-bottom. Measuring location nearest the injector section, $x = 76$ mm.

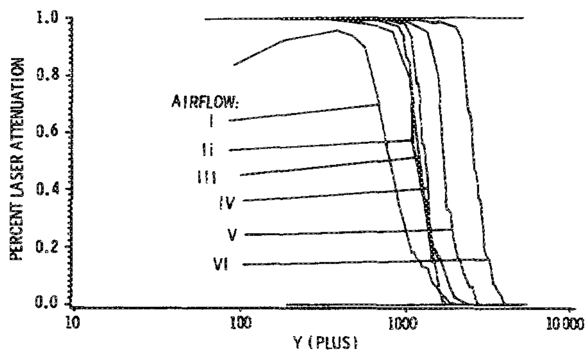

FIG. 10. Laser attenuation data as a function of y^+. Here, $u = 10.7$ m/sec; plate-on-bottom. Measuring location nearest the injector section, $x = 76$ mm.

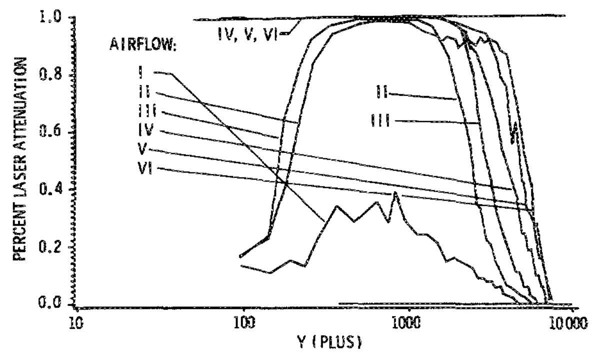

FIG. 12. Laser attenuation data as a function of y^+. Here, $u = 10.7$ m/sec; plate-on-bottom. Measuring location farthest from injector section, $x = 356$ mm.

The results at the downstream location (356 mm from the injection section) show the outer edge of the bubbles has migrated to y^+ values of several thousand for both free-stream velocities (see Figs. 11 and 12). At this downstream location, however, it is possible to measure the entire extent of the bubble cloud, particularly at the lower speed. Figure 11 shows that at all airflows the inner edge of the bubbles has moved beyond $y^+ = 200$ so that no bubbles remain in the near-wall region. At the higher speed (Fig. 12) the inner edge of the bubbles has migrated beyond $y^+ = 150$ for the three lower airflows, but is still too close to the wall to be distinguished for the higher airflows. Interestingly enough, the skin friction measurements (see Table I) show that there is virtually no C_f reduction at the downstream location for any of the airflows at the low speed, or for the three lower airflows at the higher speed. Thus, for all cases in which the inner edge of the bubble cloud has migrated past around $y^+ = 150$, there is little or no C_f reduction. At the two highest airflows at 10.7 m/sec, there remains significant reduction in C_f and Fig. 12 indicates some bubbles remain in the near-wall region. These observations suggest the bubbles must remain in the near-wall region (inside about $y^+ = 100$) to be effective C_f-reducing agents. This trend was predicted by the computational study reported in Ref. 12. Careful placement of polymers in the near-wall region have shown[17] they also must be inside the buffer layer to be effective. Resolution at sublayer scales cannot be achieved with our present measurement techniques, however, the sensitivities to microbubble location appear to be analogous.

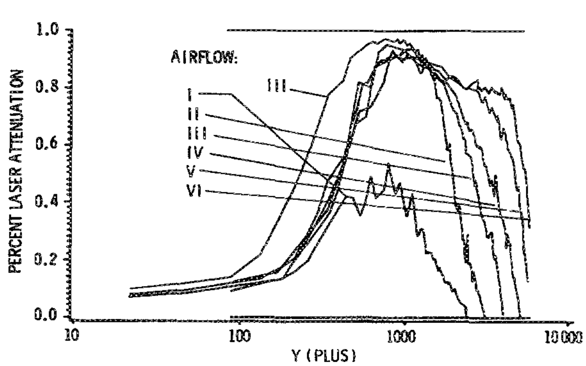

FIG. 11. Laser attenuation data as a function of y^+. Here, $u = 4.6$ m/sec; plate-on-bottom. Measuring location farthest from injector section, $x = 356$ mm.

VII. SUMMARY

Both laser transmission measurements and direct visual evidence show the existence of a clear, bubble-free region between the bubble cloud and the plate for the plate-on-bottom orientation. Within the resolution of our measurements, this clear water region does not occur for the plate-on-top orientation. Hence it is reasonable to conclude that the clear water region is the result of buoyancy, rather than viscous lift as proposed earlier.[6,8] For cases reported here in which the inner edge of the bubbles had moved to about $y^+ = 150$ there was no longer any drag reduction present. This suggests that the bubbles are effective only when they are very near the wall.

Both plate-on-bottom and plate-on-top results show that the outer edge of the bubbles spreads farther into the stream with increasing distance from the injection section and that the bubble cloud becomes correspondingly thicker. The spreading rate is faster for the plate-on-bottom configuration, demonstrating that buoyancy is a factor, but the persistence of spreading for the plate-on-top configuration where buoyancy inhibits such motion shows that turbulent diffusion is also significant. This diffusion, combined with bubble coalescence, appears to be a mechanism that leads to the reduction in effectiveness of the bubbles with distance from the injection section for the plate-on-top data. Additional measurements of the thickness of the bubble cloud for the plate-on-top orientation show that for constant airflow rate, the cloud becomes thinner as the free-stream velocity is increased, while for the same volumetric flow ratio of air to water, the cloud remains about the same size. This helps to explain the effectiveness of volumetric flow ratio normalization in collapsing the drag reduction data.[10] The effects of gravity on the plate-on-bottom data cause it to grow thicker for either constant airflow rate or air to water flow ratio, suggesting the bubbles should be more effective at higher speeds.

Finally, bubble size measurements made at low airflow rates show sizes ranging from 150–1200 μm. Simple dimensional arguments show that the order of magnitude of the bubble sizes should not change appreciably with increased drag reduction obtained at higher airflow rates. Smallest bubble sizes are some ten times the sublayer thickness while largest bubble sizes are a tenth of the boundary-layer thickness. As bubble size is only relatively weakly dependent on either surface tension or flow characteristics (dissipation, say), this may help to explain the relative insensitivity of the phenomenon to injection technique or to surfactant addition. As in the case of single pore injection, bubble size was found to increase with airflow rate and reduced velocity. In all cases, measured bubble sizes increased with distance from the injection section indicating significant coalescence was taking place.

ACKNOWLEDGEMENT

This work was sponsored by the Office of Naval Research under Contract No. N00014-81-K-0481.

[1]M. E. McCormick and R. Bhattacharyya, Nav. Eng. J. **85**, 11 (1973).

[2]G. S. Migirenko and A. R. Evseev, *Problems of Thermophysics and Physical Hydrodynamics* (Nauka, Novosibirsk, 1974) (in Russian).

[3]Yu. N. Dubnischev, E. R. Evseev, V. S. Sobolev, and E. N. Utkin, J. Appl. Mech. Tech. Phys. **16**, 114 (1975) [Zh. Prikl. Mekh. Tekh. Fiz. **1**, 147 (1975)].

[4]V. G. Bogdevich and A. G. Malyuga, in *Investigations of Boundary Layer Control*, edited by S. S. Kutateladze and G. S. Migrenko (Thermophysics Institute Publishing House, Novosibirsk, 1976) (in Russian), p. 62.

[5]V. G. Bogdevich and A. R. Evseev, in Ref. 4, p. 49.

[6]N. K. Madavan, S. Deutsch, and C. L. Merkle, Phys. Fluids **27**, 356 (1984).

[7]N. K. Madavan, S. Deutsch, and C. L. Merkle, AIAA Publ. 84-0348, 1984.

[8]N. K. Madavan, S. Deutsch, and C. L. Merkle, J. Fluid Mech. **156**, 237 (1985).

[9]S. Deutsch and J. Castano, Phys. Fluids **29**, 3590 (1986).

[10]C. L. Merkle and S. Deutsch, AIAA Publ. 85-0537, 1985.

[11]H. H. Legner, Phys. Fluids **27**, 2788 (1984).

[12]N. K. Madavan, C. L. Merkle, and S. Deutsch, J. Fluids Eng. **107**, 370 (1985).

[13]N. H. Hughes, M. M. Reischman, and J. M. Holzman, in *Proceedings of the Sixth Biennial Symposium on Turbulence* (University of Missouri, Rolla, 1979), p. 274.

[14]E. Silberman, in *Proceedings of the Fifth Midwestern Conference on Fluid Mechanics* (University of Michigan, Ann Arbor, MI, 1957), p. 263.

[15]J. O. Hinze, AIChE J. **1**, 289 (1955).

[16]R. M. Thomas, Int. J. Multiphase Flow **7**, 709 (1981).

[17]W. G. Tiederman, T. S. Luchik, and D. G. Bogard, J. Fluid Mech. **156**, 419 (1985).